Geophysical Research Letters

Key Points:

- A sequence of discrete structures within an interplanetary coronal mass ejection sheath are tracked via multipoint measurements
- Each structure results in magnetospheric compression, adiabatic enhancement of ions and electrons, and cyclotron wave growth
- This event highlights the importance of fine-scale solar wind structure and sheath regions for driving dayside magnetospheric phenomena

Correspondence to:

L. W. Blum,
lauren.blum@lasp.colorado.edu

Prompt Response of the Dayside Magnetosphere to Discrete Structures Within the Sheath Region of a Coronal Mass Ejection

L. W. Blum[1,2] ![ORCID], A. Koval[3,4], I. G. Richardson[3,5] ![ORCID], L. B. Wilson[3] ![ORCID], D. Malaspina[1,2] ![ORCID], A. Greeley[3] ![ORCID], and A. N. Jaynes[6] ![ORCID]

[1]Department of Astrophysical and Planetary Sciences, CU Boulder, Boulder, CO, USA, [2]Laboratory for Atmospheric and Space Physics, CU Boulder, Boulder, CO, USA, [3]NASA Goddard Space Flight Center, Greenbelt, MD, USA, [4]University of Maryland Baltimore County, Baltimore, MD, USA, [5]Department of Astronomy, University of Maryland, College Park, MD, USA, [6]Department of Physics and Astronomy, University of Iowa, Iowa City, IA, USA

Abstract A sequence of discrete solar wind structures within the sheath region of an interplanetary coronal mass ejection on November 6, 2015, caused a series of compressions and releases of the dayside magnetosphere. Each compression resulted in a brief adiabatic enhancement of ions (electrons) driving bursts of electromagnetic ion cyclotron (EMIC; whistler mode chorus) wave growth across the dayside magnetosphere. Fine-structured rising tones were observed in the EMIC wave bursts, resulting in nonlinear scattering of relativistic electrons in the outer radiation belt. Multipoint observations allow us to study the spatial structure and evolution of these sheath structures as they propagate Earthward from L1 as well as the spatio-temporal characteristics of the magnetospheric response. This event highlights the importance of fine-scale solar wind structure, in particular within complex sheath regions, in driving dayside phenomena within the inner magnetosphere.

Plain Language Summary On November 6, 2015, a sequence of abrupt changes in Earth's magnetic field and the associated conditions in the solar wind were observed. Multispacecraft observations allow us to study both the spatial structure and evolution of the solar wind structures that impacted the Earth, as well as the response of Earth's magnetic field and particles trapped within it. The fine-scale structures observed in the solar wind are demonstrated to produce distinct magnetospheric particle distributions and wave excitation. This event highlights the importance of fine-scale solar wind structure in driving magnetospheric phenomena.

1. Introduction

Solar wind structures act as critical drivers of magnetospheric dynamics, resulting in wave generation, magnetospheric reconfigurations, and geomagnetic storms. Magnetospheric responses, including particles and waves, to large-scale structures such as interplanetary (IP) shocks, interplanetary coronal mass ejections (ICMEs), and co-rotating interaction regions (CIRs) have been studied for decades. In particular, IP shocks have been shown to produce magnetosonic pulses that can propagate through the magnetosphere and resonate with MeV electrons, leading to particle acceleration and distinct drift echo signatures (e.g., Hudson et al., 2017; Kanekal et al., 2016; Li et al., 1993; Schiller et al., 2016). Shocks can also drive strong global ultralow frequency (ULF) waves (e.g., Hao et al., 2019; Kivelson & Southwood, 1985; Zhang et al., 2020), which can subsequently modulate magnetospheric particle populations as well as other active wave modes (e.g., Malaspina et al., 2015).

Pressure gradients in the ambient solar wind are another mechanism that can result in magnetospheric wave generation. Periodic density structures, often observed in the slow solar wind, can drive ULF wave activity in the magnetosphere at similar frequencies to those in the solar wind (Kepko et al., 2002; Kepko & Spence, 2003). These ULF waves can then modulate particles and other wave modes within the magnetosphere. Breneman et al. (2020) observed modulation of hiss waves throughout the plasmasphere induced by solar wind pressure variations and a "forced breathing" of the magnetosphere. These waves resulted in MeV electron precipitation, also showing ULF modulation. Liu et al. (2019) found quasi-periodic electromagnetic ion cyclotron (EMIC) wave activity in the outer dayside magnetosphere as a result of ULF wave

compressions, again driven by variation in the solar wind dynamic pressure. Finally, pressure pulses in the solar wind, whether associated with shocks, ICMEs, CIRs, or more moderate variations of ambient solar wind, can generate cyclotron wave growth in the magnetosphere. A number of studies have explored the occurrences of EMIC waves driven by solar wind pressure pulses, particularly in the outer dayside magnetosphere (e.g., Chen et al., 2019; Cho et al., 2016; Olson & Lee, 1983; Usanova et al., 2008, 2012).

ICME sheaths, the turbulent regions of compressed, heated plasma that form ahead of ICME ejecta, have gained attention for their effects on wave excitation and radiation belt dynamics. Recent studies have investigated the role of various regions of ICMEs in driving different radiation belt responses (Hietala et al., 2014; Kilpua, Fontaine, et al., 2019; Kilpua, Turner, et al., 2019; Turner et al., 2019). Kalliokoski et al. (2020) found that sheaths tended to produce enhanced EMIC and Pc5 ULF wave power as compared to ejecta and were associated with depletions in >1 MeV electron populations at $L > 4$. The enhanced density, temperature, and flow pressure typically found in sheath regions can result in a compressed magnetopause as well as increased ULF wave activity, leading to loss of energetic electrons both through the magnetopause as well as via precipitation into the atmosphere (Kilpua et al., 2017).

Here, we explore the effects of fine structure within an ICME sheath that impacted Earth's magnetosphere on November 6, 2015. Utilizing multipoint observations in the upstream solar wind and dayside magnetosphere, we examine the Earthward propagation of a sequence of density and magnetic field structures in the sheath region. Each structure resulted in a compression of the dayside magnetosphere, adiabatic enhancement of ions and electrons, and subsequent bursts of EMIC wave activity. The sheath's impact on both particles and waves throughout the inner magnetosphere is presented as well as the effects of these EMIC waves on energetic particles in the outer radiation belt. These observations suggest a close association between structures in the sheath, geomagnetic activity, and magnetospheric wave activity, to be explored further in this study.

2. Observations

To study the event on November 6, 2015, we combine measurements from a number of different observatories throughout the magnetosphere and upstream solar wind. Data sources include: solar wind parameters compiled from near-Earth spacecraft as provided by the OMNI database (https://omniweb.gsfc.nasa.gov/html/HROdocum.html); vector magnetic field and thermal plasma measurements (where available) from the Advanced Composition Explorer (ACE) (Smith et al., 1998), Deep Space Climate Observatory (DSCOVR) (https://www.nesdis.noaa.gov/content/dscovr-deep-space-climate-observatory), Wind (Lepping et al., 1995; Lin et al., 1995) and Acceleration, Reconnection, Turbulence, and Electrodynamics of the Moon's Interaction with the Sun (ARTEMIS) spacecraft (Angelopoulos, 2010; Auster et al., 2008; McFadden et al., 2008); high-resolution magnetic field measurements from Geostationary Operational Environmental Satellite (GOES) 13 and 15 (Singer et al., 1996); survey mode vector magnetic field measurements from the Fluxgate Magnetometer (FGM) (Torbert et al., 2016) on Magnetospheric Multiscale (MMS) (Burch et al., 2016); fluxgate and search coil magnetometer measurements from the Electric and Magnetic Field Instrument Suite and Integrated Science (EMFISIS) (Kletzing et al., 2013) on the Van Allen Probes (refered to subsequently as RBSP A and B; Mauk et al., 2013) and ion and electron measurements from Radiation Belt Storm Probes Ion Compostion Experiment (RBSPICE; Mitchell et al., 2013), Helium Oxygen Proton and Electron (HOPE; Funsten et al., 2013), Magnetic Electron Ion Spectrometer (MagEIS; Blake et al. 2013), and Relativistic Electron-Proton Telescope (REPT) instruments (Baker et al., 2013).

2.1. Solar Wind Structures

At 18:16 UT on November 6, 2015, an IP shock at the leading edge of the sheath region of an ICME impacted the magnetosphere, followed by a geomagnetic storm early on November 7. Figure 1 shows the (1a) interplanetary magnetic field (IMF) B_{total}, (1b) IMF B_z, (1c) solar wind flow speed, (1d) proton density, (1e) temperature, (1f) dynamic pressure, from the OMNI data set in which parameters have been shifted to the nose of the bow shock, and finally (1g) Sym-H, a measure of the disturbance of midlatitude geomagnetic field, similar to the Dst index, often used to identify geomagnetic storms. The sheath-ejecta boundary is indicated by the cyan line at 06:45 UT on November 7, the ejecta having the enhanced, slowly rotating,
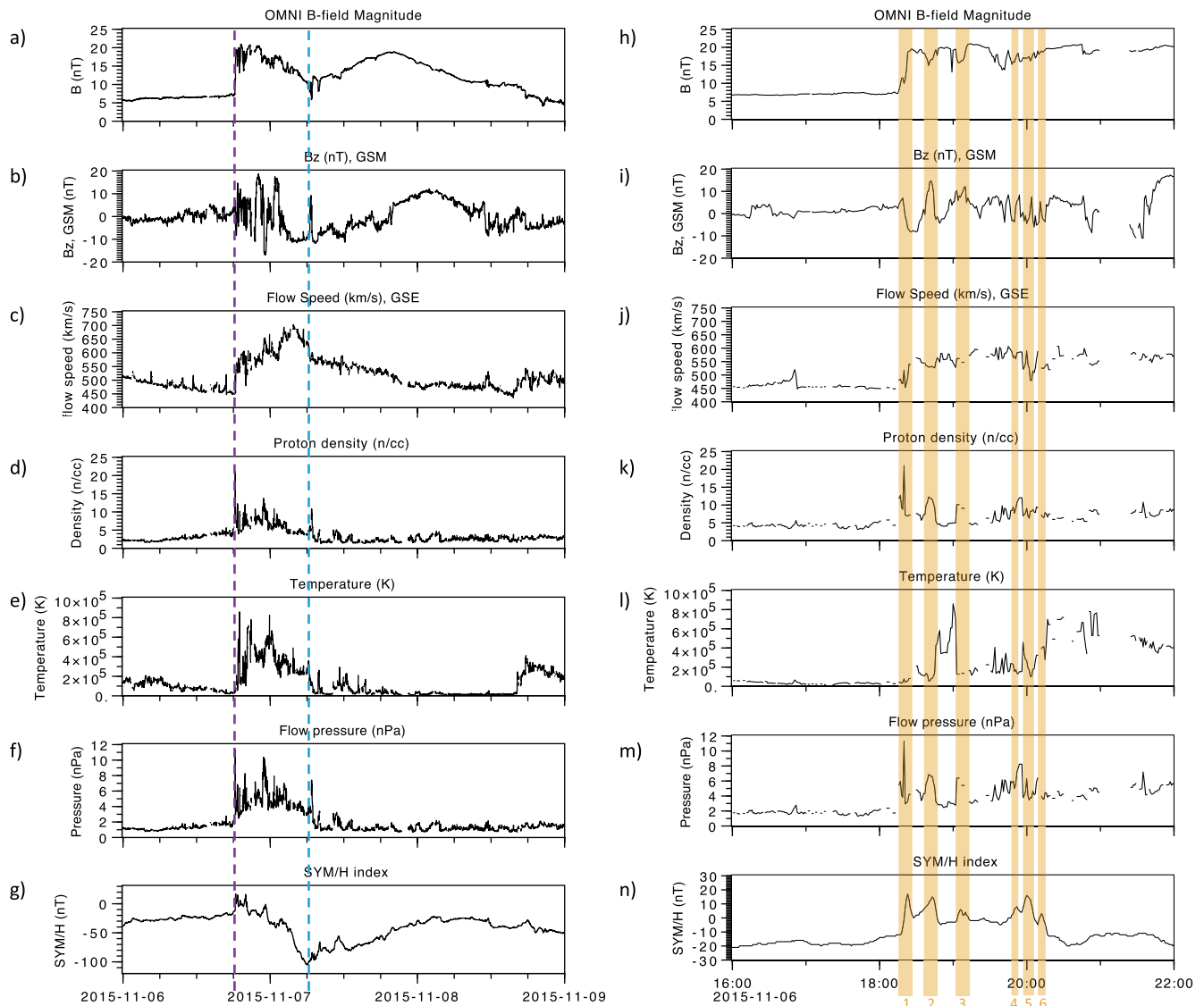
Figure 1. Solar wind properties, as provided by the OMNI database and propagated to the nose of the bow shock, and the Sym-H index. (a–g) Measurements from November 6 to November 9, 2016, while (h–n) focus in from 16:00 to 22:00 UT on November 6. The magenta line at 18:16 UT marks the time of shock arrival, cyan line at 06:45 UT the boundary between ICME sheath and ejecta, and shaded orange regions on the right panels mark six positive Sym-H excursions to be investigated further in this study.

flux-rope-like magnetic field characteristic of a "magnetic cloud" (Klein & Burlaga, 1982). The shock at the leading edge of the sheath, marked by the magenta line, is associated with abrupt increases in the magnetic field strength, flow speed, density, and temperature. The sheath properties are consistent with those typically measured in such regions, namely higher densities and plasma beta, as well as frequent discontinuities presumably due to the accumulation of plasma and magnetic field from different sources as the ICME propagates through the solar wind (e.g., Kilpua et al., 2017). Roughly six distinct sudden Sym-H increases (marked by the shaded orange regions in 1n) occurred between the initial positive excursion associated with storm sudden commencement and the main phase of the geomagnetic storm. Each was associated with changes in solar wind parameters—typically (1h) decrease in B_{total}, (1i) a turning of IMF B_z, and (1k) increase in density. The impact of these six features on magnetospheric dynamics will be explored in subsequent sections.

Figures 2a–2d present the three-component magnetic field in Geocentric Solar Ecliptic (GSE) coordinates as measured by L1 spacecraft and ARTEMIS ThC, with spacecraft locations illustrated in Figure 2e. ACE,
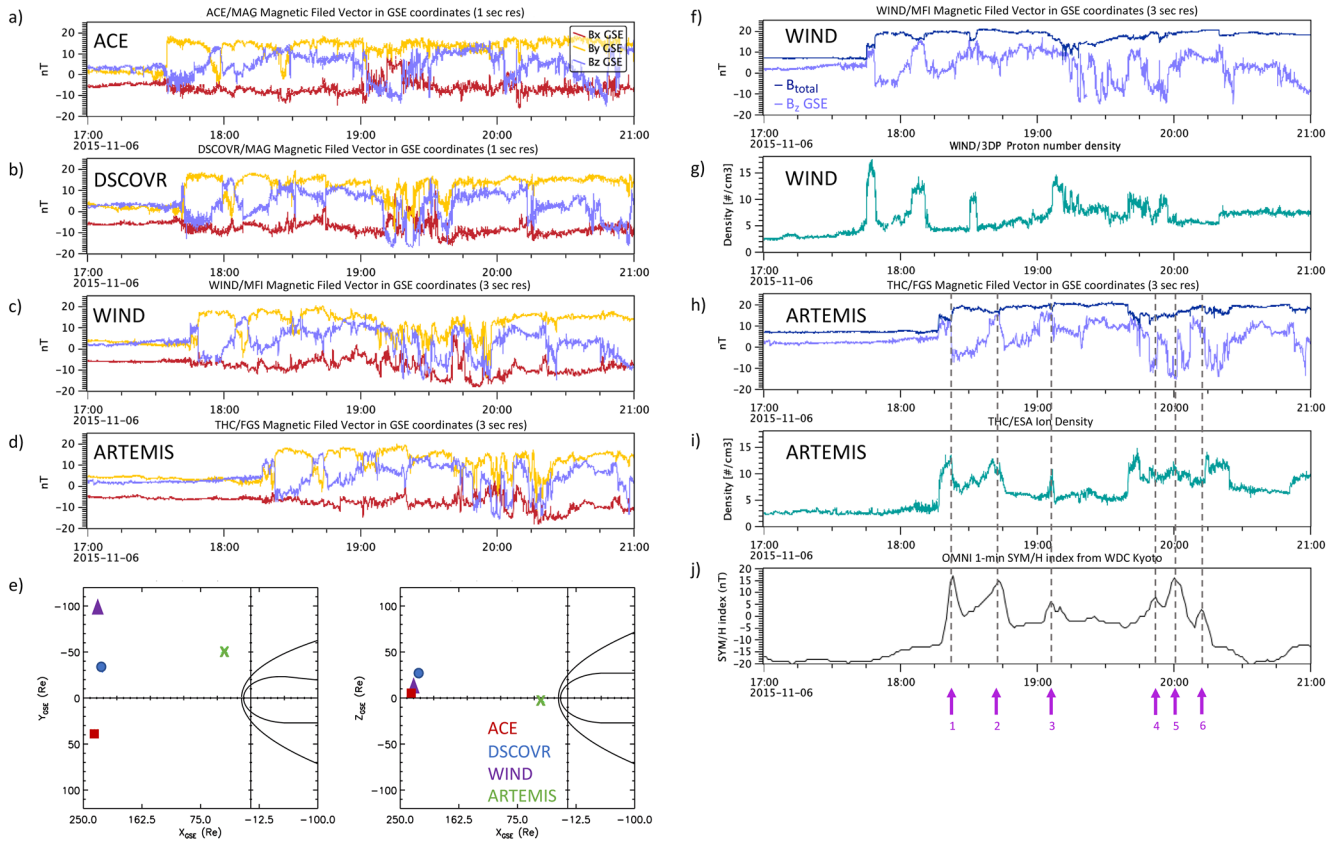
Figure 2. (a–d) Vector magnetic field measurements from ACE, DSCOVR, Wind, and ARTEMIS in the upstream solar wind. (e) Spacecraft locations in GSE coordinates at 18 UT on November 6. (f and h) B_{total} and B_z as well as (g and i) ion density at Wind and ARTEMIS, respectively. (j) Sym-H, with vertical dashed lines marking the peaks of the six positive excursions.

DSCOVR, and Wind are closely aligned in x_GSE and span ~150 Earth radii (R_E) in y_GSE. Following the initial shock, which arrived first at ACE, clear magnetic field discontinuities showing very similar fine-scale structure propagated past all four spacecraft, with the first three structures (the first being the shock) passing ACE at 17:35, 17:55, and 18:25 UT, and reaching ARTEMIS around 18:17, 18:39, and 19:01 UT. Shock parameters at Wind are estimated to be $n = [−0.937, −0.348, −0.030]$ GSE, $V_{shock} = 578.4$ km/s, Theta_$B_n = 47°$, and Mf = 1.9 using a least-squares fit of the full set of Rankine-Hugoniot conservation equations to the magnetic field and thermal plasma measurements (e.g., Koval & Szabo, 2008, 2010; Szabo, 1994). Based on estimates of the shock normal and propagation speed at Wind, the intersection time at the bow shock should be ~18:15:38—53 UTC and intersection point at [12.11, 10.03, 0.79] R_E GSE. The shock arrival time in the OMNI data is in good agreement with this estimate as well as with the arrival time observed by ARTEMIS at 18:17 UT. A tangential discontinuity (TD) formed following the shock (~4 min after at Wind and 6 min after at ARTEMIS). This has Theta_B_n almost 90° on both sides, propagating with the flow and in pressure balance on both sides ($n = [−0.812, −0.421, −0.404]$ GSE, $V_{TD} = 483.5$ km/s).

Figures 2f–2i present B_{total}, B_z, and ion density n at Wind and ARTEMIS, the spacecraft for which thermal plasma measurements are available, as well as (Figure 2j) Sym-H for timing comparison. The first three structures are once again clearly distinguishable, with distinct density enhancements corresponding to changes in B_z and small depletions in B_{total}. The first structure is bounded by the shock and TD and the second and third structures are each bounded by a pair of TDs with $n = [−0.858, −0.363, −0.364]$ GSE, $V_{TD} = 512.4$ km/s and $n = [−0.834, −0.419, −0.360]$ GSE, $V_{TD} = 509.8$ km/s for the second structure and $n = [−0.832, −0.519, −0.196]$ GSE, $V_{TD} = 529.9$ km/s and $n = [−0.681, 0.049, −0.731]$ GSE, $V_{TD} = 441.6$ km/s for the third structure. The double-peak of the third Sym-H excursion is mirrored in the B_z profile at Wind (Figure 4f). Structures 4–6 are less easily distinguished in the density measurements but are still associated with discrete B_z discontinuities and nonetheless produce clear positive Sym-H signatures of similar
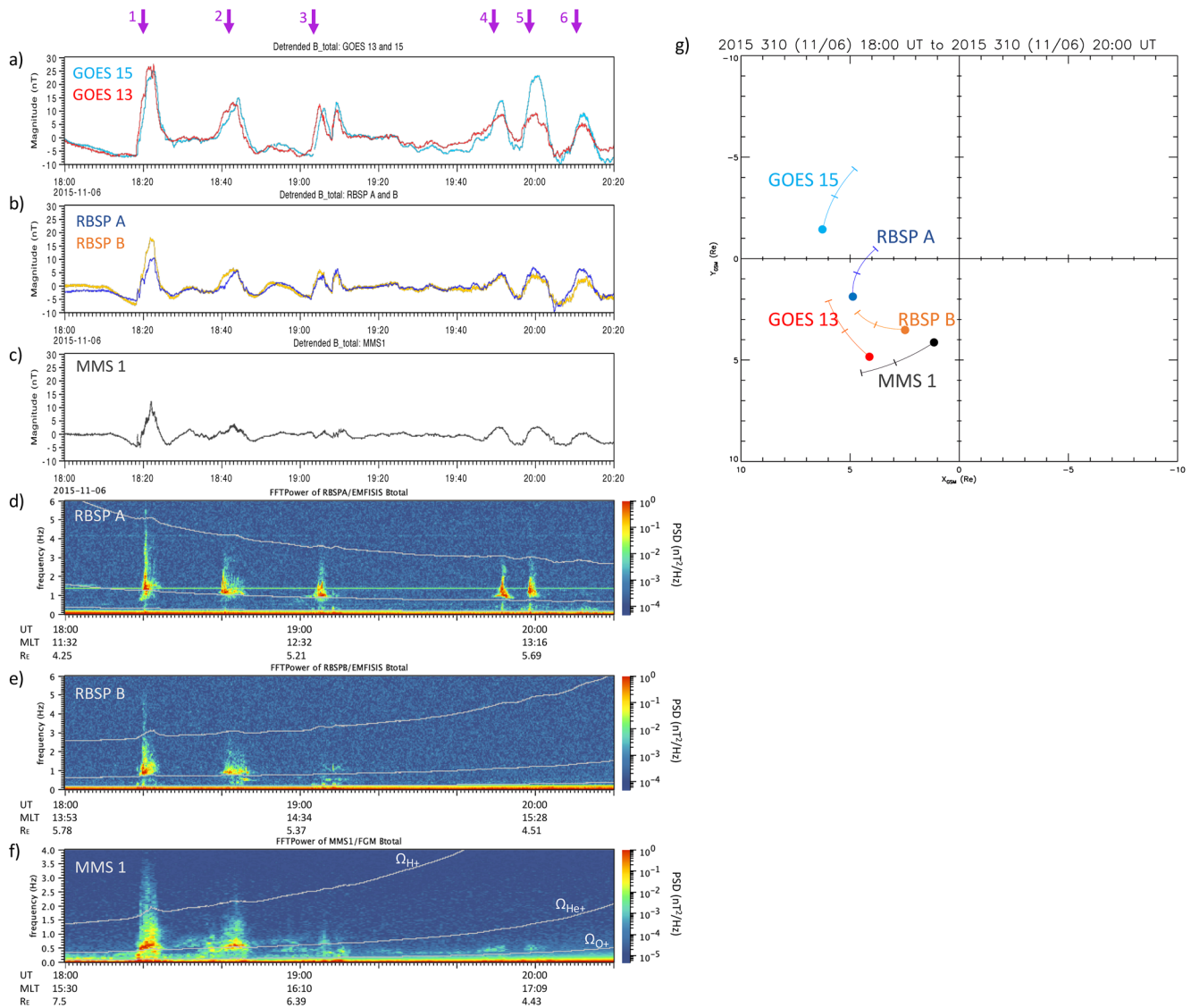
Figure 3. (a–c) Detrended magnetic field measurements at GOES 13 and 15, RBSP A and B, and MMS 1, respectively. (d–f) Magnetic field spectrograms showing bursts of EMIC wave activity at RBSP A, B, and MMS 1. White lines indicate the local H+, He+, and O+ cyclotron frequencies. (g) The location of these five spacecraft from 18:00 to 20:00 UT, with filled circles indicating the location at 20:00 UT.

magnitude to structures 1–3. This difference between the properties and magnitude of the structures observed at Wind and ARTEMIS as compared to the response of the magnetosphere could be due to propagation effects and structure evolution over time and space, or to a different combination of variables resulting in similar dynamic pressure and compression of the magnetopause.

2.2. Magnetospheric Response

From 18:20 to 20:20 UT on November 6, a sequence of magnetic field compressions and bursts of EMIC wave activity were observed by multiple spacecraft on the dayside magnetosphere in response to the solar wind structures investigated in Section 2.1. Figure 3 shows (3a–c) the detrended magnetic field at GOES 13 and 15, RBSP A and B, and MMS 1, respectively, (3d–f) magnetic field spectrograms from RBSP A, B, and MMS 1, as well as (3g) the locations of these spacecraft during this time. A train of magnetic field disturbances were observed at all five spacecraft, with each corresponding to the impact of a sheath structure and positive Sym-H signature from the previous section. The proximity of the spacecraft to the subsolar point
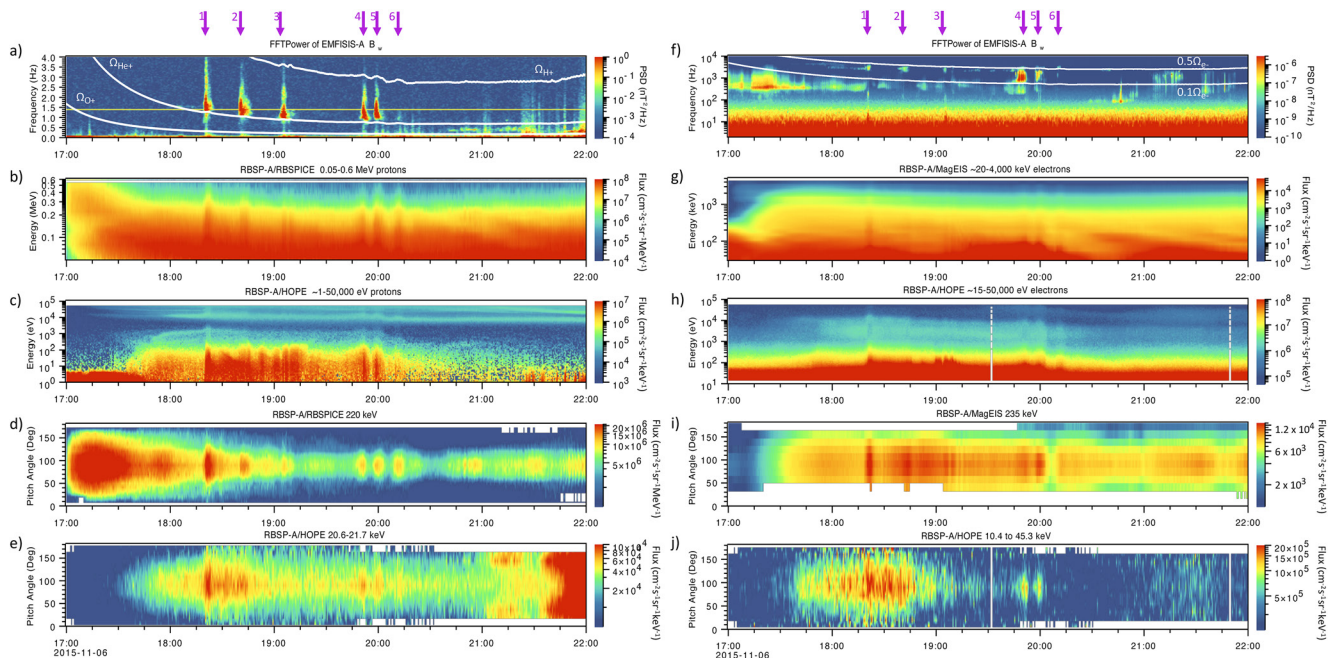
Figure 4. Plasma and wave measurements from RBSP A. (a and f) Magnetic field spectrograms of EMIC and whistler-mode waves, respectively, with white lines indicating the local H+, He+, O+ ion and 0.5, 0.1× electron cyclotron frequencies. (b and c) Proton and (g and h) electron energy spectra spanning eV–100s keV energies. (d and e) Proton and (i and j) electron pitch angle distributions taken at two example energies ~20 and ~200 keV, showing 90° peaked distributions during the compressions, as marked by the magenta arrows.

influenced the compression signature each observed—for example, GOES 15 observed larger compressions than GOES 13 around 20 UT, while the disturbance at 18:20 UT was of similar magnitude or slightly larger at GOES 13. These signatures are consistent with the location of the shock impact at the magnetopause, just downward of the subsolar point, as estimated in Section 2.1. Coincident with these magnetic field compressions, simultaneous bursts of EMIC waves were observed by the RBSP and MMS spacecraft. GOES magnetic field sampling of 0.512 samples/s is unable to resolve these ~1–2 Hz waves. Again, the wave signatures vary depending on spacecraft location, with the more dusk-ward spacecraft (e.g., RBSP B and MMS) primarily observing the first three wave bursts, while RBSP A, closer to noon, saw additional bursts later in the period. Each compression was brief, lasting only a few minutes, and resulted in a correspondingly short burst of wave activity, turning on and off near-simultaneously across the spacecraft spanning multiple R_E across the dayside magnetosphere. During the first two wave bursts, the spacecraft spanned radial distances of ~4.5–7 R_E and 11:30–15:30 MLT, and by the fifth burst at 20:00 UT, which was primarily observed by RBSP A only, the spacecraft spanned 4.4–5.7 R_E radially and more dusk-side local times from 13 to 17 MLT.

In addition to the geomagnetic field and waves, magnetospheric particles responded to the impact of the sheath structures. Figure 4 shows the wave and particle observations at RBSP A (similar electron and ion signatures are observed at RBSP B, MMS, and GOES, not shown). Panels (4b) and (4c) show proton energy spectrograms from the RBSPICE and HOPE instruments, respectively, collectively spanning energies from eV through 100s keV. Adiabatic enhancements across a wide range of energies were observed at each of the six wave bursts, with particle fluxes increasing during magnetic field compressions and relaxing to previous levels as the magnetic field returned to baseline. Pitch angle distributions at two example proton energies, (4d) ~20 keV and (4e) ~200 keV, reveal that the flux enhancements during the magnetospheric compressions were peaked at 90° across a large range of energies, consistent with adiabatic enhancement as well as with anisotropic conditions leading to cyclotron wave growth ($T_{perpendicular} > T_{parallel}$) (e.g., Cornwall, 1965; Gary, 1993). Xue et al. (2021) showed that these ion distributions provided sufficient free energy to produce the observed EMIC wave spectrum, based on linear theory. Figures 4f–4j show a similar scenario occurring in the eV–100s keV electron population and the resulting whistler-mode chorus waves generated by these anisotropic electron distributions. Dayside compressions, driven by enhanced solar wind dynamic pressure, have long been studied as a source of both EMIC and whistler-mode waves (e.g., McCollough et al., 2012;
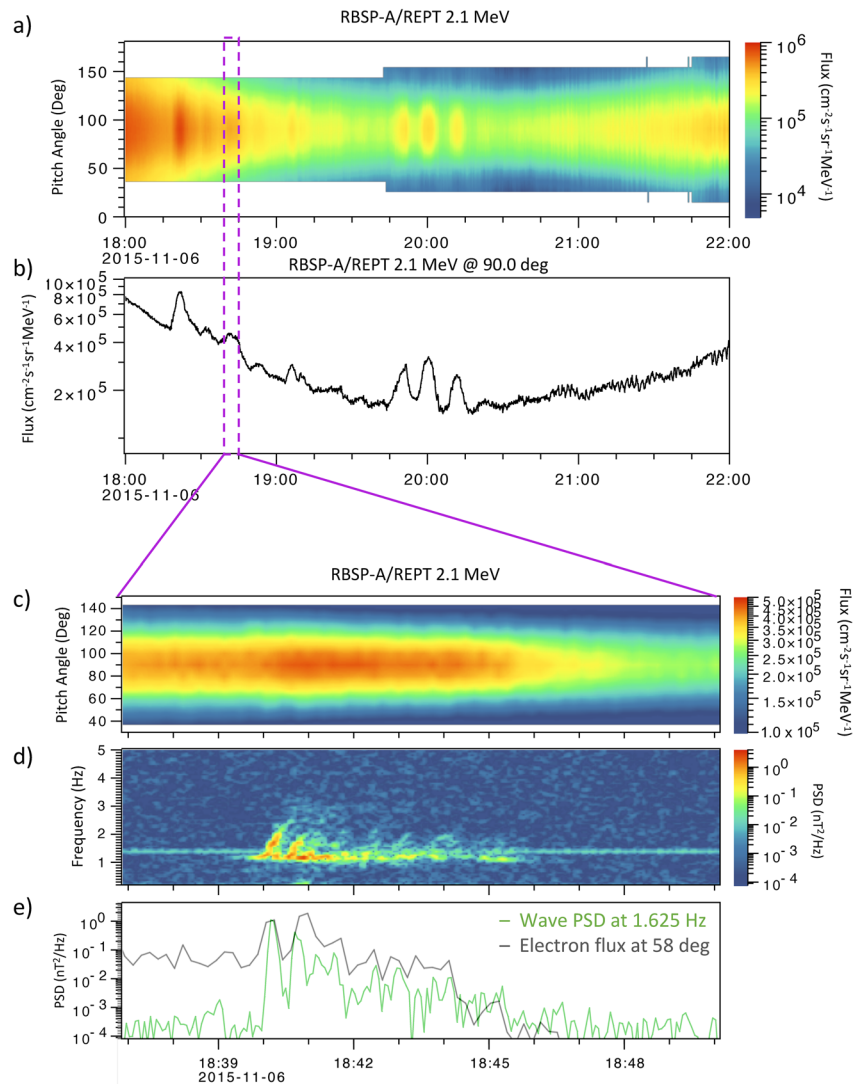
Figure 5. (a) Pitch angle distributions of 2.1 MeV electrons from 18:00 to 22:00 UT, as measured by REPT on RBSP A and (b) a slice through the distribution at 90°. (c–e) A zoom in on a ~13-min period during the second compression, showing (c) 2.1 MeV electron pitch angle distributions and (d) structured EMIC waves, with (e) electron enhancements toward lower pitch angles coincident with the first two EMIC rising tones.

Tsurutani & Smith, 1977; Usanova et al. 2012). Compression of the magnetic field leads to betatron acceleration of locally trapped ions and electrons, generating anisotropic distributions that can provide the free energy for cyclotron wave growth (e.g., Anderson & Hamilton, 1993; Kennel & Petschek, 1966). We note that in this event the durations of the compressions and subsequent releases, corresponding to the sharp turning on and off of waves, were much shorter (<a few minutes) than most previous observations of compression-driven waves, which are more often 10s of minutes to hours (Cho et al., 2016; Engebretson et al., 2015; Usanova et al., 2008).

Finally, we examine the effects of these brief but intense waves on higher-energy MeV radiation belt electrons. During this event the impact of the initial IP shock, sheath-region fine structure, resultant electromagnetic waves, and larger-scale geomagnetic storm all combined to act upon relativistic electrons, making it challenging to disentangle the various effects of these different processes. However, we can examine the local response of MeV electron pitch angle distributions in coordination with high-resolution wave measurements. Figure 5a shows the pitch angle distribution of 2.1 MeV electrons as measured by REPT on RBSP A during a 4-h period around the time of interest, with Figure 5b showing a slice through the particle

distribution at 90°. Both the adiabatic response of MeV electrons (e.g., at 18:20, 18:40 UT), as well as drift echoes due to the initial shock (e.g., at 18:30 UT) can be observed. To focus on the wave effects rather than those of the shock and geomagnetic storm, Figure 5c shows the pitch angle distribution during the second EMIC wave burst around 18:40 UT. Rising tone emissions are visible within this wave burst (Figure 5d), as have been observed previously during intense EMIC wave events (e.g., Grison et al., 2016; Nakamura et al., 2014; Pickett et al., 2010). Figure 5e shows a slice through both the wave power spectral density (green), taken at ~1.6 Hz near the peak amplitude of the first rising tone, as well as through the 2.1 MeV pitch angle distribution at off-90° (gray), taken at ~58° here as fluxes drop off steeply at lower pitch angles and REPT does not measure pitch angles below 37° during this period, due to the configuration of the background magnetic field vector relative to instrument field-of-view. Faint enhancements of MeV particles at these lower pitch angles are observed, coinciding with the first two EMIC wave rising tones (Figure 5e). These can also be seen at 1.8 and 2.6/3.4 MeV (not shown), but the signal as measured by REPT gets very weak at energies beyond this. Similar signatures were observed by Zhu et al. (2020) and shown to be a result of nonlinear interaction between rising tone EMIC waves and MeV electrons, which can scatter particles toward the loss cone via phase trapping. Kurita et al. (2018) also observed scattering of lower pitch angle MeV electrons in association with EMIC wave activity. This event suggests that while short-lived, these structured EMIC wave bursts can have rapid nonlinear scattering effects on energetic electrons, as demonstrated theoretically by Omura and Zhao (2012).

3. Discussion and Summary

On November 6, 2015, a sequence of structures in the sheath region of an ICME impacted the magnetosphere, each causing distinct responses in magnetospheric particles and waves. Multipoint observations allow us to track the propagation of these structures through the solar wind as well as their effects across the dayside inner magnetosphere. Sheath regions are generally associated with enhanced density and variable magnetic fields but in this event the near-shock sheath was made up of discrete density structures and magnetic field discontinuities that contributed to the almost periodic sequence of six magnetospheric compressions. The first three structures all seem to be of similar origin, bounded by tangential discontinuities, while the latter three are less clearly distinguished in the density measurements but still associated with distinct magnetic field discontinuities. While the cause of these structures is unknown and a topic for future investigations, their impacts on the magnetosphere are explored here. Each structure caused an abrupt compression and release of the dayside magnetosphere, strongest near the location of shock impact. Adiabatic enhancements of ions and electrons were produced in response, with profiles following the magnetic field compression profiles. These anisotropic plasma distributions resulted in near-instantaneous turning on and off of EMIC and chorus waves. Such compression-driven EMIC waves have been observed in a number of past studies. Fuselier et al. (2004) observed transient detached proton aurora across the dayside in response to IP shocks and attributed these to ion scattering by EMIC waves. One such event mapped to a region from 11 to 15 MLT and 5 to 8 R_E, similar to the spatial extent observed in this event, and the authors found that shock impact angle related to whether aurora (and EMIC waves) were generated on the dusk or dawn side. Utilizing multipoint measurements, Engebretson et al. (2015, 2018) found EMIC waves spanning the entire dayside magnetosphere in response to sharp solar wind dynamic pressure enhancements and Blum et al. (2017) found wave extents to be more often larger on the dayside than nightside. The observations here are consistent with these studies and suggest dayside EMIC waves driven by solar wind compressions often span large spatial extents (~3–4 R_E and hours MLT) and have durations directly driven by variations in solar wind dynamic pressure.

While short-lived, the EMIC waves observed on November 6 were of large amplitude and contained rising tones, which can result in nonlinear scattering of radiation belt electrons. A number of recent studies have investigated the role of ICME sheaths in driving different radiation belt responses (e.g., Kilpua, Fontaine, et al., 2019; Kilpua, Turner, et al., 2019; Turner et al., 2019). In superposed epoch studies, Hietala et al. (2014) and Kalliokoski et al. (2020) found enhanced magnetospheric wave power as well as depletions in MeV electron populations during sheath regions, and Kilpua, Turner, et al. (2019) found near-shock sheath regions to be the most geoeffective. What superposed epoch studies do not reveal is the high amount of complexity and localized discontinuities within sheaths that may be a driver of wave and plasma

variability. This study demonstrates that discrete structures within sheaths can produce distinct magnetospheric responses in both particles and waves and should be considered when exploring the response of the radiation belts to ICMEs. This event highlights the importance of fine-scale solar wind structure and complex sheath regions in driving dayside magnetospheric phenomena not just close to the magnetopause but deep within the inner magnetosphere, generating particle and wave signatures spanning large spatial regions with temporal durations dictated by the solar wind driver.

Data Availability Statement

All measurements utilized in this study can be found at the following websites: https://satdat.ngdc.noaa.gov/sem/goes/data/science/mag/ for GOES 13 and 15 magnetometer data and https://cdaweb.gsfc.nasa.gov/index.html/ for all else, by selecting the following spacecraft instruments and data products: ACE_MFI; ARTEMIS THC_FGM and ESA; DSCOVR_MAG; MMS1_FGM; Van Allen Probes_HOPE, MAGEIS, REPT, RBSPICE and MAGNETOMETER; Wind_MFI and 3DP; and OMNI_1MIN.

References

Anderson, B. J., & Hamilton, D. C. (1993). Electromagnetic ion cyclotron waves stimulated by modest magnetospheric compressions. *Journal of Geophysical Research*, *98*. 11369–11382. https://doi.org/10.1029/93ja00605

Angelopoulos, V. (2010). The ARTEMIS mission. *Space Science Reviews*, *165*, 3–25. https://doi.org/10.1007/s11214-010-9687-2

Auster, H. U., Glassmeier, K. H., Magnes, W., Aydogar, O., Baumjohann, W., Constantinescu, D., et al. (2008). The THEMIS fluxgate magnetometer. *Space Science Reviews*, *141*, 235–264. https://doi.org/10.1007/s11214-008-9365-9

Baker, D. N., Kanekal, S. G., Hoxie, V. C., Batiste, S., Bolton, M., Li, X., Elkington, S. R., et al (2013). The Relativistic Electron-Proton Telescope (REPT) instrument on board the Radiation Belt Storm Probes (RBSP) spacecraft: Characterization of Earth's radiation belt high-energy particle populations. *Space Science Reviews*. *179*, 337–381. https://doi.org/10.1007/s11214-012-9950-9

Blake, J. B., Carranza, P. A., Claudepierre, S. G., Clemmons, J. H., Crain, W. R., Dotan, Y., et al. (2013). The Magnetic Electron Ion Spectrometer (MagEIS) instruments aboard the Radiation Belt Storm Probes (RBSP) spacecraft. *Space Science Reviews*, *179*, 383–421. https://doi.org/10.1007/s11214-013-9991-8

Blum, L. W., Bonnell, J. W., Agapitov, O., Paulson, K., & Kletzing, C. (2017). EMIC wave scale size in the inner magnetosphere: Observations from the dual Van Allen Probes. *Geophysical Research Letters*, *44*, 1227–1233. https://doi.org/10.1002/2016GL072316

Breneman, A. W., Halford, A. J., Millan, R. M., Woodger, L. A., Zhang, X. J., Sandhu, J. K., et al. (2020). Driving of outer belt electron loss by solar wind dynamic pressure structures: Analysis of balloon and satellite data. *Journal of Geophysical Research: Space Physics*, *125*. https://doi.org/10.1029/2020JA028097

Burch, J. L., Moore, T. E., Torbert, R. B., & Giles, B. L. (2016). Magnetospheric Multiscale overview and science objectives. *Space Science Reviews*, *199*, 5–21. https://doi.org/10.1007/s11214-015-0164-9

Chen, H., Gao, X., Lu, Q., & Wang, S. (2019). Analyzing EMIC waves in the inner magnetosphere using long-term Van Allen Probes observations. *Journal of Geophysical Research: Space Physics*, *124*, 7402–7412. https://doi.org/10.1029/2019JA026965

Cho, J.-H., Lee, D.-Y., Noh, S.-J., Shin, D.-K., Hwang, J., Kim, K.-C., et al. (2016). Van Allen Probes observations of electromagnetic ion cyclotron waves triggered by enhanced solar wind dynamic pressure. *Journal of Geophysical Research: Space Physics*, *121*, 9771–9793. https://doi.org/10.1002/2016JA022841

Cornwall, J. M. (1965). Cyclotron instabilities and electromagnetic emission in the ultra low frequency and very low frequency ranges. *Journal of Geophysical Research*, *70*, 61–69. https://doi.org/10.1029/JZ070i001p00061

Engebretson, M. J., Posch, J. L., Capman, N. S. S., Campuzano, N. G., Bělik, P., Allen, R. C., et al. (2018). MMS, Van Allen Probes, GOES 13, and ground-based magnetometer observations of EMIC wave events before, during, and after a modest interplanetary shock. *Journal of Geophysical Research: Space Physics*, *123*, 8331–8357. https://doi.org/10.1029/2018JA025984

Engebretson, M. J., Posch, J. L., Wygant, J. R., Kletzing, C. A., Lessard, M. R., Huang, C.-L., et al. (2015). Van Allen Probes, NOAA, GOES, and ground observations of an intense EMIC wave event extending over 12 h in magnetic local time. *Journal of Geophysical Research: Space Physics*, *120*, 5465–5488. https://doi.org/10.1002/2015JA021227

Funsten, H. O., Skoug, R. M., Guthrie, A. A., MacDonald, E. A., Baldonado, J. R., Harper, R. W., et al. (2013). Helium, Oxygen, Proton, and Electron (HOPE) mass spectrometer for the radiation belt storm probes mission. *Space Science Reviews*, *179*, 423–484. https://doi.org/10.1007/s11214-013-9968-7

Fuselier, S. A., Gary, S. P., Thomsen, M. F., Claflin, E. S., Hubert, B., Sandel, B. R., & Immel, T. (2004). Generation of transient dayside subauroral proton precipitation. *Journal of Geophysical Research*, *109*, A12227. https://doi.org/10.1029/2004JA010393

Gary, S. P. (1993). *Theory of space plasma microinstabilities*. Cambridge University Press. https://doi.org/10.1017/cbo9780511551512

Grison, B., Darrouzet, F., Santolík, O., Cornilleau-Wehrlin, N., & Masson, A. (2016). Cluster observations of reflected EMIC-triggered emission. *Geophysical Research Letters*, *43*. https://doi.org/10.1002/2016GL069096

Hao, Y. X., Zong, Q. G., Zhou, X. Z., Rankin, R., Chen, X. R., Liu, Y., et al. (2019). Global-scale ULF waves associated with SSC accelerate magnetospheric ultrarelativistic electrons. *Journal of Geophysical Research: Space Physics*, *124*, 1525–1538. https://doi.org/10.1029/2018JA026134

Hietala, H., Kilpua, E. K. J., Turner, D. L., & Angelopoulos, V., (2014). Depleting effects of ICME-driven sheath regions on the outer electron radiation belt. *Geophysical Research Letters*, *41*, 2258–2265. https://doi.org/10.1002/2014GL059551

Hudson, M., Jaynes, A., Kress, B., Li, Z., Patel, M., Shen, X. C., et al. (2017). Simulated prompt acceleration of multi-MeV electrons by the 17 March 2015 Interplanetary shock. *Journal of Geophysical Research: Space Physics*, *122*(10), 10036–10046. https://doi.org/10.1002/2017JA024445

Kalliokoski, M. M. H., Kilpua, E. K. J., Osmane, A., Turner, D. L., Jaynes, A. N., Turc, L., et al. (2020). Outer radiation belt and inner magnetospheric response to sheath regions of coronal mass ejections: A statistical analysis. *Annales Geophysicae*, *38*, 683–701. https://doi.org/10.5194/angeo-38-683-2020

Kanekal, S. G., Baker, D. N., Fennell, J. F., Jones, A., Schiller, Q., Richardson, I. G., et al. (2016). Prompt acceleration of magnetospheric electrons to ultrarelativistic energies by the 17 March 2015 interplanetary shock. *Journal of Geophysical Research: Space Physics*, *121*, 7622–7635. https://doi.org/10.1002/2016JA022596

Kennel, C. F., & Petschek, H. E. (1966). Limit on stably trapped particle fluxes. *Journal of Geophysical Research*, *71*(1), 1–28. https://doi.org/10.1029/JZ071i001p00001

Kepko, L., & Spence, H. E. (2003). Observations of discrete, global magnetospheric oscillations directly driven by solar wind density variations. *Journal of Geophysical Research*, *108*, 1257. https://doi.org/10.1029/2002JA009676

Kepko, L., Spence, H. E., & Singer, H. J. (2002). ULF waves in the solar wind as direct drivers of magnetospheric pulsations. *Geophysical Research Letters*, *29*(8), 1197. https://doi.org/10.1029/2001GL014405

Kilpua, E. K. J., Fontaine, D., Moissard, C., Ala-Lahti, M., Palme-rio, E., Yordanova, E., et al. (2019). Solar wind properties and geospace impact of coronal mass ejection-driven sheath regions: Variation and driver dependence. *Space Weather*, *17*, 1257–1280. https://doi.org/10.1029/2019SW002217

Kilpua, E. K. J., Koskinen, H. E. J., & Pulkkinen, T. I. (2017). Coronal mass ejections and their sheath regions in interplanetary space. *Living Reviews in Solar Physics*, *14*, 5. https://doi.org/10.1007/s41116-017-0009-6

Kilpua, E. K. J., Turner, D. L., Jaynes, A. N., Hietala, H., Koskinen, H. E. J., Osmane, A., et al. (2019). Outer Van Allen radiation belt response to interacting interplanetary corronal mass ejections. *Journal of Geophysical Research: Space Physics*, *124*, 1927–1947. https://doi.org/10.1029/2018JA026238

Kivelson, M. G., & Southwood, D. J. (1985). Resonant ULF waves – A new interpretation. *Geophysical Research Letters*, *12*, 49–52. https://doi.org/10.1029/gl012i001p00049

Klein, L. W., & Burlaga, L. F. (1982). Interplanetary magnetic clouds at 1 AU. *Journal of Geophysical Research*, *87*, 613–624. https://doi.org/10.1029/JA087iA02p00613

Kletzing, C. A., Kurth, W. S., Acuna, M., MacDowall, R. J., Torbert, R. B., Averkamp, T., et al (2013). The Electric and Magnetic Field Instrument Suite and Integrated Science (EMFISIS) on RBSP. *Space Science Reviews*, *179*, 127–181. https://doi.org/10.1007/s11214-013-9993-6

Koval, A., & Szabo, A. (2008). Modified "Rankine-Hugoniot" shock fitting technique: Simultaneous solution for shock normal and speed. *Journal of Geophysical Research*, *113*, A10110. https://doi.org/10.1029/2008JA013337

Koval, A., & Szabo, A. (2010). Multispacecraft observations of interplanetary shock shapes on the scales of the Earth's magnetosphere. *Journal of Geophysical Research*, *115*, A12105. https://doi.org/10.1029/2010JA015373

Kurita, S., Miyoshi, Y., Shiokawa, K., Higashio, N., Mitani, T., Takashima, T., et al. (2018). Rapid loss of relativistic electrons by EMIC waves in the outer radiation belt observed by Arase, Van Allen Probes, and the PWING ground stations. *Geophysical Research Letters*, *45*. 12720–12729. https://doi.org/10.1029/2018GL080262

Lepping, R. P., Acũna, M. H., Burlaga, L. F., Farrell, W. M., Slavin, J. A., Schatten, K. H., et al (1995). The WIND magnetic field investigation. *Space Science Reviews*, *71*, 207–229. https://doi.org/10.1007/BF00751330

Lin, R. P., Anderson, K. A., Ashford, S., Carlson, C., Curtis, D., Ergun, R., et al (1995). A three-dimensional plasma and energetic particle investigation for the wind spacecraft. *Space Science Reviews*, *71*, 125–153. https://doi.org/10.1007/BF00751328

Liu, S., Xia, Z., Chen, L., Liu, Y., Liao, Z., & Zhu, H. (2019). Magnetospheric Multiscale Observation of quasiperiodic EMIC waves associated with enhanced solar wind pressure. *Geophysical Research Letters*, *46*, 7096–7104. https://doi.org/10.1029/2019GL083421

Li, X., Roth, I., Temerin, M., Wygant, J., Hudson, M., & Blake, J. (1993). Simulation of the prompt energization and transport of radiation belt particles during the March 24, 1991 SSC. *Geophysical Research Letters*, *20*(22), 2423–2426. https://doi.org/10.1029/93GL02701

Malaspina, D. M., Claudepierre, S. G., Takahashi, K., Jaynes, A. N., Elkington, S. R., Ergun, R. E., et al. (2015). Kinetic Alfvén waves and particle response associated with a shock-induced, global ULF perturbation of the terrestrial magnetosphere. *Geophysical Research Letters*, *42*. https://doi.org/10.1002/2015GL065935

Mauk, B. H., Fox, N. J., Kanekal, S. G., Kessel, R. L., Sibeck, D. G., Ukhorskiy, A. (2013). Science objectives and rationale for the radiation belt storm probes mission. *Space Science Reviews*, *179*, 3–27. https://doi.org/10.1007/s11214-012-9908-y

McCollough, J. P., Elkington, S. R., & Baker, D. N. (2012). The role of Shabansky orbits in compression-related electromagnetic ion cyclotron wave growth. *Journal of Geophysical Research*, *117*, A01208. https://doi.org/10.1029/2011JA016948

McFadden, J. P., Carlson, C. W., Larson, D., Angelopoulos, V., Ludlam, M., Abiad, R., et al. (2008). The THEMIS ESA plasma instrument and in-flight calibration. *Space Science Reviews*. *141*, 277–302. https://doi.org/10.1007/s11214-008-9440-2

Mitchell, D. G., Lanzerotti, L. J., Kim, C. K., Stokes, M., Ho, G., Cooper, S., et al., (2013). Radiation Belt Storm Probes Ion Composition Experiment (RBSPICE). *Space Science Reviews*, https://doi.org/10.1007/s11214-013-9965-x

Nakamura, S., Omura, Y., Machida, S., Shoji, M., Nosé, M., & Angelopoulos, V. (2014). Electromagnetic ion cyclotron rising tone emissions observed by THEMIS probes outside the plasmapause. *Journal of Geophysical Research: Space Physics*, *119*, 1874–1886. https://doi.org/10.1002/2013JA019146

Olson, J. V., & Lee, L. C. (1983). Pc1 wave generation by sudden impulses. *Planetary and Space Science*, *31*, 295–302. https://doi.org/10.1016/0032-0633(83)90079-X

Omura, Y., & Zhao, Q. (2012). Nonlinear pitch angle scattering of relativistic electrons by emic waves in the inner magnetosphere. *Journal of Geophysical Research*, *117*, A08227. https://doi.org/10.1029/2012JA017943

Pickett, J. S., Grison, B., Omura, Y., Engebretson, M. J., Dandouras, I., Masson, A., et al (2010). Cluster observations of EMIC triggered emissions in association with Pc1 waves near Earth's plasmapause. *Geophysical Research Letters*, *37*, L09104. https://doi.org/10.1029/2010GL042648

Schiller, Q., Kanekal, S. G., Jian, L. K., Li, X., Jones, A., Baker, D. N., et al. (2016). Prompt injections of highly relativistic electrons induced by interplanetary shocks: A statistical study of Van Allen Probes observations, *Geophysical Research Letters*, *43*(24). 12317–12324. https://doi.org/10.1002/2016GL071628

Singer, H., Matheson, L., Grubb, R., Newman, A., & Bouwer, D. (1996). Monitoring space weather with the GOES magnetometers. In E. R. Washwell, (Ed.), Society of Photo-Optical Instrumentation Engineers (SPIE) Conference Series (Vol. 2812, pp. 299–308). Society of Photo-Optical Instrumentation Engineers.

Smith, C., L'Heureux, J., Ness, N., Acuña, M. H., Burlaga, L. F., & Scheifele, J. (1998). The ACE magnetic fields experiment. *Space Science Reviews*, *86*, 613–632. https://doi.org/10.1023/A:1005092216668

Szabo, A. (1994). An improved solution to the "Rankine-Hugoniot" problem. *Journal of Geophysical Research*, *99*, 14737–14746. https://doi.org/10.1029/94JA00782

Torbert, R. B., Russell, C. T., Magnes, W., Ergun, R. E., Lindqvist, P. -A., LeContel, O., et al (2016). The FIELDS instrument suite on MMS: Scientific objectives, measurements, and data products. *Space Science Reviews*, *199*, 105–135. https://doi.org/10.1007/s11214-014-0109-8

Tsurutani, B. T., & Smith, E. J. (1977). Two types of magnetospheric ELF chorus and their substorm dependences. *Journal of Geophysical Research*, *82*(32), 5112–5128. https://doi.org/10.1029/JA082i032p05112

Turner, D. L., Kilpua, E. K. J., Hietala, H., Claudepierre, S. G., O'Brien, T. P., Fennell, J. F., et al. (2019). The response of Earth's electron radiation belts to geomagnetic storms: Statistics from the Van Allen Probes era including effects from different storm drivers. *Journal of Geophysical Research: Space Physics*, *124*, 1013–1034. https://doi.org/10.1029/2018JA026066

Usanova, M. E., Mann, I. R., Bortnik, J., Shao, L., & Angelopoulos, V. (2012). THEMIS observations of electromagnetic ion cyclotron wave occurrence: Dependence on AE, SYMH, and solar wind dynamic pressure. *Journal of Geophysical Research*, *117*, A10218. https://doi.org/10.1029/2012JA018049

Usanova, M. E., Mann, I. R., Rae, I. J., Kale, Z. C., Angelopoulos, V., Bonnell, J. W., et al. (2008). Multi-point observations of magnetospheric compression-related EMIC Pc1 waves by THEMIS and CARISMA. *Geophysical Research Letters*, *35*, L17S25. https://doi.org/10.1029/2008GL034458

Xue, Z., Yuan, Z., & Yu, X. (2021). Prompt emergence and disappearance of EMIC waves driven by the sequentially enhanced solar wind dynamic pressure. *Geophysical Research Letters*, *48*, e2020GL091479. https://doi.org/10.1029/2020gl091479

Zhang, D., Liu, W., Li, X., Sarris, T. E., Wang, Y., Xiao, C., et al. (2020). Relation between shock-related impulse and subsequent ULF wave in the Earth's magnetosphere. *Geophysical Research Letters*, *47*(23). https://doi.org/10.1029/2020GL090027

Zhu, H., Chen, L., Claudepierre, S. G., & Zheng, L. (2020). Direct evidence of the pitch angle scattering of relativistic electrons induced by EMIC waves. *Geophysical Research Letters*, *47*, e2019GL085637. https://doi.org/10.1029/2019GL085637